Science Advances
AAAS

Supplementary Materials for

Ion sensing with single charge resolution using sub–10-nm electrical double layer–gated silicon nanowire transistors

Qitao Hu, Si Chen, Paul Solomon*, Zhen Zhang*

*Corresponding author. Email: zhen.zhang@angstrom.uu.se (Z.Z.); solomonp@us.ibm.com (P.S.)

Published 3 December 2021, *Sci. Adv.* **7**, eabj6711 (2021)
DOI: 10.1126/sciadv.abj6711

This PDF file includes:

Supplementary Text
Figs. S1 to S14
Table S1
References

Supplementary Section 1: Device fabrication process flow

An optimized top-down process was used to fabricate the SiNWFET devices. The fabrication process is presented step by step in Fig. S1.

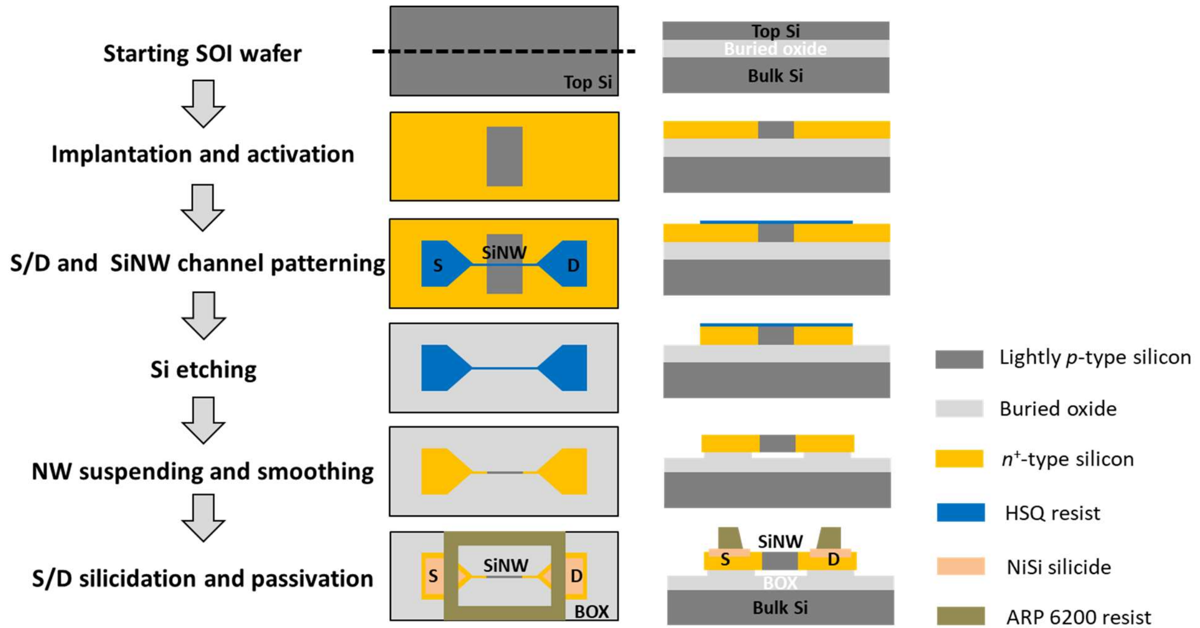

Fig. S1. Fabrication process flow of the SiNWFET device. The top-view and cross-sectional schematic illustrations of the device at each step are presented. The dashed line in the top-view schematic indicates the position of cross-sectional cut.

Supplementary Section 2: Fabrication process optimization

Some optimized steps in the fabrication flow were illustrated in the scanning electron microscope (SEM) images in Fig. S2. Firstly, in S/D heavily implantation process, the channel was protected by the negative electron beam lithography (EBL) resist UVN. The resolution of UVN is roughly 300 nm (Fig. S2a), which defines the minimum length of NW to be 400 nm, including 50-nm-long margins on both sides for misalignment control. However, 400-nm-long SiNW will collapse or break when all processes are done. Therefore, the width of UVN implantation structure was reduced to the minimum level of 80 nm (Fig. S2b) by the improved EBL dose modulation. Secondly, in the EBL exposure of S/D pads and NW channel, the dose of NW channel was much higher than that of S/D pads. Given the short NW length, the S/D pads were in proximity to each other, thus the high dose of NW overlapped with the dose of S/D pads would expose the nearby resist between S/D pads as indicated by the overdose issue in Fig. S2c. To solve this problem, the patterns of S/D pads were narrowed and NW-pad double exposure strategy was used to suppress the overlapped dose. Fig. S2d presents a well-defined transistor pattern. Thirdly, although the double expose succeeded avoiding the proximity issue, the poor alignment between NW and S/D pads exposure appeared as a new concern (Fig. S2e). The quality of alignment mark for EBL exposure was improved to control the misalignment in an accepted range (Fig. S2f).

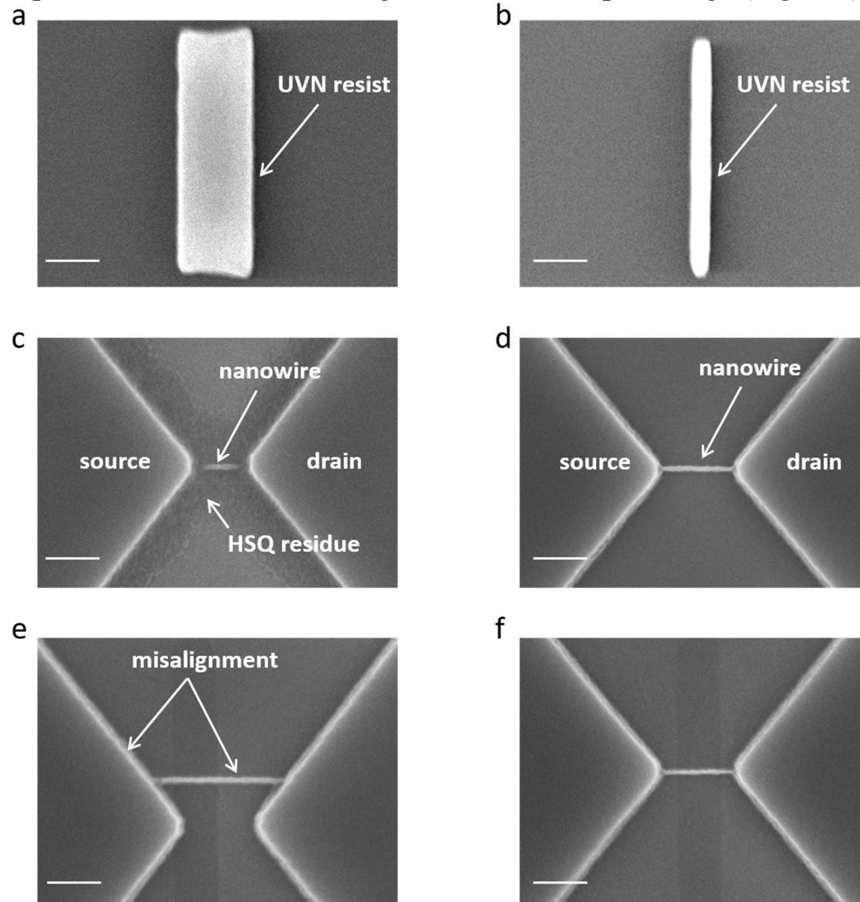

Fig. S2. SiNW transistors fabrication optimization. SEM images of UVN pattern by the (a) typical and (b) optimized exposure parameters. Proximity issue of the (c) non-optimized and (d) optimized exposure process. Misalignment of the (e) non-optimized and (f) optimized exposure process. The scale bar is 200 nm.

Supplementary Section 3: Intrinsic device noise of SiNWFET

The intrinsic noise of a traditional MOSFET is mainly generated by the carrier trapping/detrapping process near the gate oxide/channel interface (*18-20*). The intrinsic noise consists of both carrier number (ΔN) and mobility ($\Delta\mu$) fluctuation components. ΔN is associated with the number fluctuation of carriers in the device channel due to carrier trapping/detrapping near the gate oxide/channel interface, while $\Delta\mu$ is related to Coulomb scattering near the interface. The distribution of traps in the gate oxide accounts for the $1/f$-like intrinsic noise spectrum. The intrinsic noise amplitude is inversely proportional to the gate area.

In our gate-oxide-free SiNWFETs, the electrical double layer acts as the gate dielectric layer. The defects on the SiNW surface are the source for the intrinsic noise and their distribution in the energy domain could also lead to $1/f$-like noise spectrum. Despite the difference in device structure, the intrinsic noise of our device also follows the gate area dependence as it is generated by the uncorrelated surface defects (*38*). As a result, the intrinsic noise the gate-oxide-free SiNWFETs will increase with downsizing due to the reduction of gate area, which is a serious concern for our SiNWFETs when they are applied for single charge detections.

Supplementary Section 4: H_2 annealing process

The SiNW surface gets smoothened and the surface defects are eliminated after the annealing in the H_2 ambient. The SEM images of SiNW with and without H_2 annealing are presented in Fig. S3.

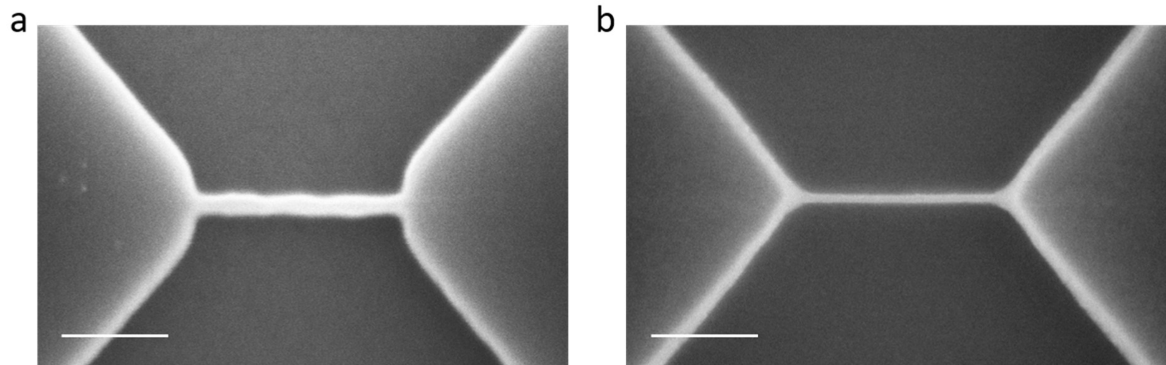

Fig. S3. SiNW process optimization with H_2 annealing. SEM images of SiNWs (a) with and (b) without H_2 annealing process. The scale bar is 100 nm.

Supplementary Section 5: Transfer characteristics comparison of the SiNWFETs with and without H_2 annealing

Transfer curves of 10 SiNWFET devices with and without H_2 annealing are plotted in Fig. S4. H_2 annealing greatly improved *SS* and reduced device-to-device variation.

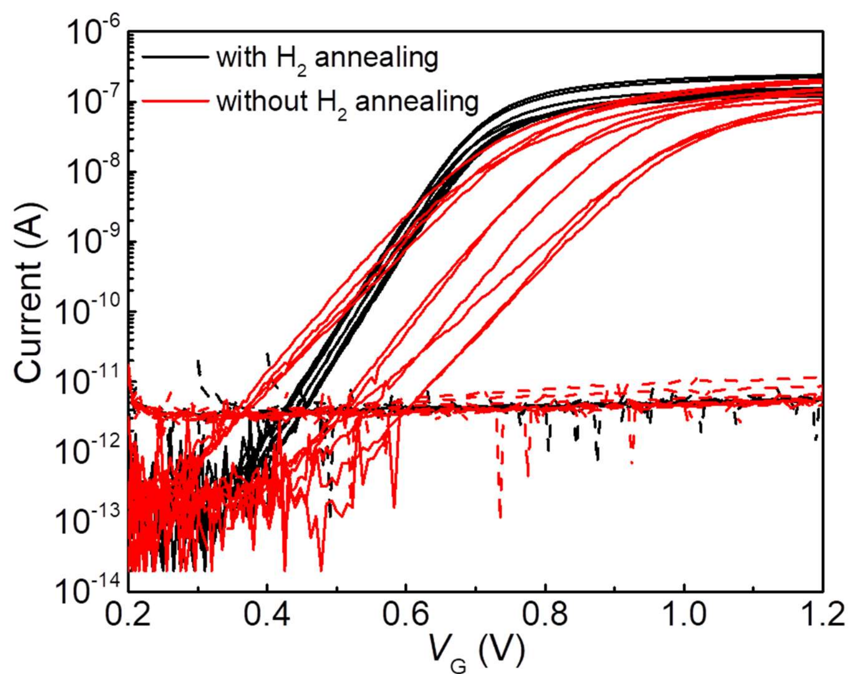

Fig. S4. Transfer curves of SiNWFETs with (black) and without (red) H_2 annealing measured in 1 mM KCl at V_{DS} = 10 mV.

Supplementary Section 6: Output characteristics of the H_2-annealed SiNWFET

The output characteristics of the SiNWFET with H_2 annealing measured in 1 mM KCl are shown in Fig. S5. The device shows a good Ohmic contact performance.

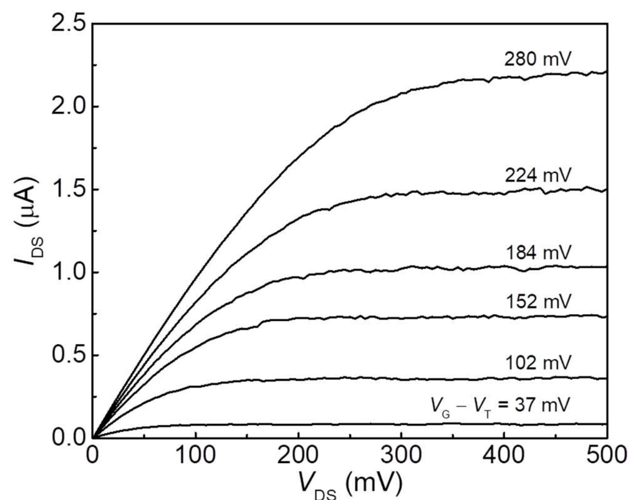

Fig. S5. Output characteristics of the H_2-annealed SiNWFET. The reference electrode voltages are marked in the figures.

Supplementary Section 7: Intrinsic noise comparison of the SiNWFETs with and without H_2 annealing

Area-normalized gate voltage noises of 10 SiNWFETs (I_{DS} = 1, 5, 10, 50, and 100 nA) with and without H_2 annealing are plotted in Fig. S6. Both of them have 1/*f*-like noise, but the noise of SiNWFETs without H_2 annealing is ~10 times higher.

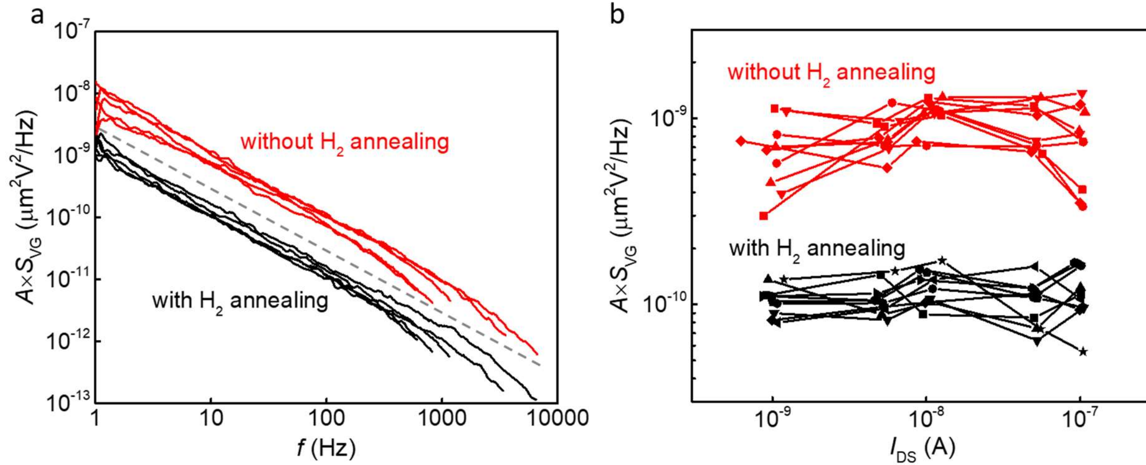

Fig. S6. Area-normalized gate voltage noises. (a) PSD of normalized gate voltage noise and (b) 10 Hz normalized gate voltage noise at different drain currents of the SiNWFETs with and without H_2 annealing measured in 1 mM KCl at V_{DS} = 10 mV. The dashed line in (a) is a 1/*f* reference line.

Supplementary Section 8: *p*H response of the H_2-annealed SiNWFET

The *p*H response generated by Si-OH group on the SiNW surface can be analyzed using site-binding and Gouy-Chapman-Stern (GCS) models. The surface reactions between H^+ ion in liquid and Si-OH group on SiNW are

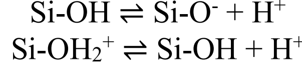

Their dissociation constants are denoted as K_a and K_b, respectively. The dynamic equilibrium between H^+ ion and Si-OH group is capable to buffer the change of surface H^+ concentration c_{Hs}. The intrinsic buffer capacity β_{int} depends on the surface site density N_{OH} (*34*):

$$\beta_{int} = N_{OH} \frac{K_b c_{Hs}^2 + 4K_a K_b c_{Hs} + K_a K_b^2}{\left(K_a K_b + K_b c_{Hs} + c_{Hs}^2\right)^2} 2.3 c_{Hs} . \quad \text{(S1)}$$

The *p*H response of SiNWFET corresponds to the change of surface potential $\Delta\varphi_s$, which can be expressed as (*34*)

$$\frac{\Delta\varphi_s}{\Delta p\mathrm{H}_b} = -2.3\alpha \frac{kT}{q}, \text{ with } \alpha = \frac{1}{\frac{2.3kTC_{EDL}}{q^2\beta_{int}} + 1}, \quad \text{(S2)}$$

where $p\mathrm{H}_b$ is the bulk *p*H value, k is the Boltzmann constant, T is the temperature, q is the elemental charge, and C_{EDL} is the capacitance of electrical double layer, respectively. The *p*H response of the H_2-annealed SiNWFET can be well fitted by the equations S1 and S2 (see Fig. S7), from which the effective surface site density is extracted as $N_{OH} = 6\times10^{13}$ cm^{-2}.

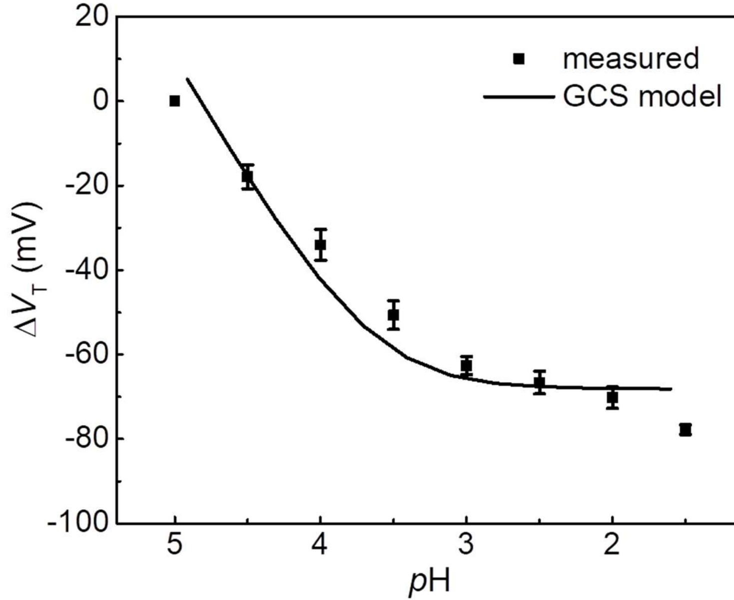

Fig. S7. *p*H response of the H_2-annealed SiNWFET. The *p*H values were changed by changing the HCl concentrations. The solid curve is the fitted results by GCS model with the effective –OH group density to be 6×10^{13} cm^{-2}.

Supplementary Section 9: Current histograms of Dev. A at different $V_G - V_T$

The current histograms of Dev. A are presented in Fig. S8, where two Gaussian peaks are clearly separated at each histogram. The areas of the two current peaks indicate the relative probabilities of filled and empty dangling bond (DB) states.

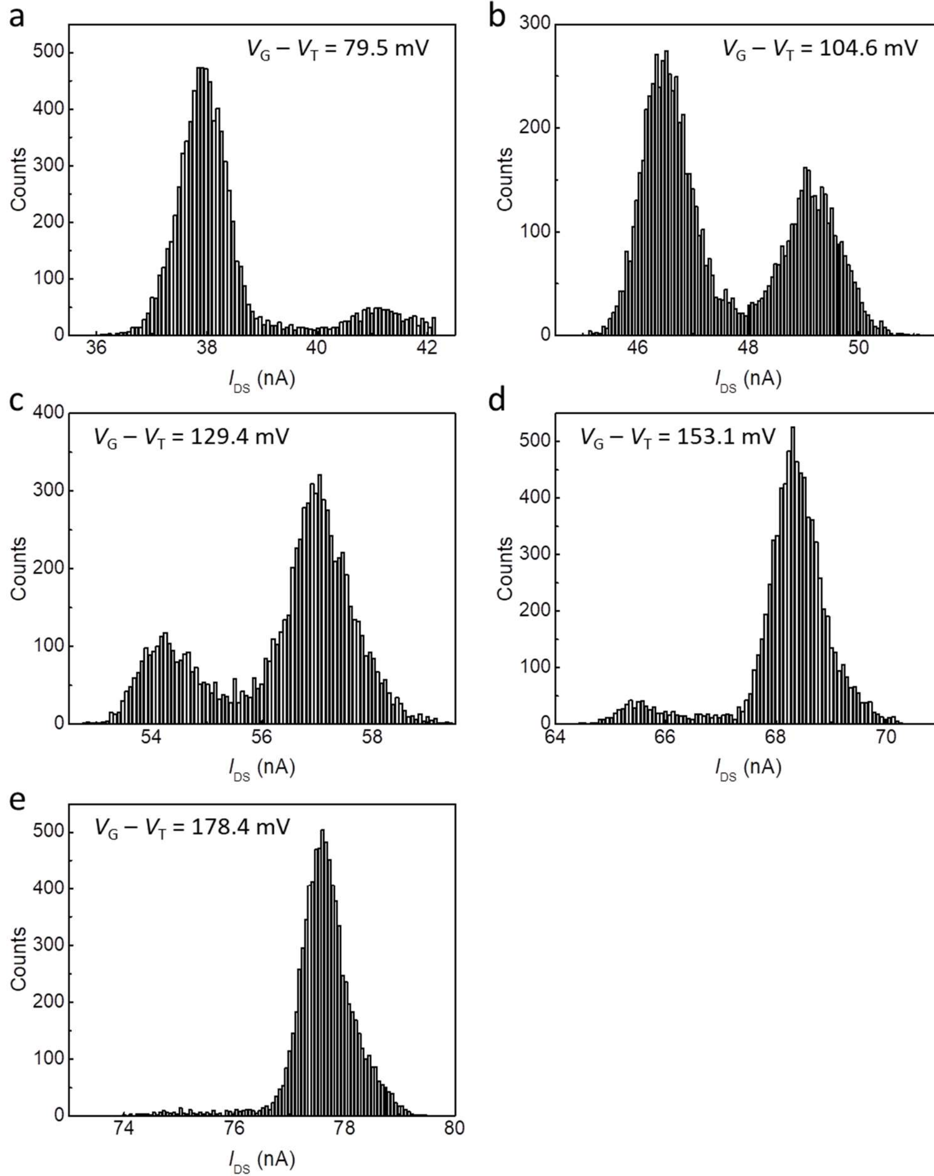

Fig. S8. Histograms of current records listed in Fig. 3A.

Supplementary Section 10: Trap occupation probability of Dev. A and Dev. B

The trap occupation probability P can be calculated by $A_h/(A_h + A_l)$, where A_h and A_l are the peak areas of high and low current states, respectively.

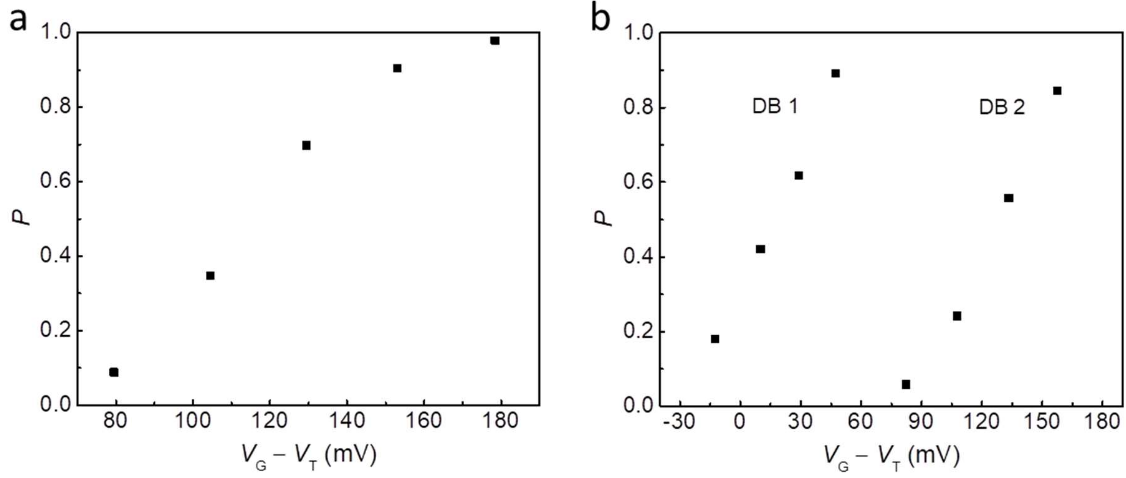

Fig. S9. Transition of trap occupation probability. Trap occupation probability of (a) Dev. A and (b) Dev. B at different gate overdrive $V_G - V_T$.

Supplementary Section 11: PSD of time-traces of Dev. A

The corner frequency f_c is determined as

$$f_c = \frac{1}{2\pi}\left(\frac{1}{\tau_c} + \frac{1}{\tau_e}\right) = \frac{1}{2\pi}\left(k_{on}c_{Hs} + k_{off}e^{-qV_{st}/kT}\right), \tag{S3}$$

where k_{on} and k_{off} are the association and dissociation constant of single H^+-DB interaction, respectively, c_{Hs} the surface H^+ concentration, q the elementary charge, V_{st} the potential drop across Stern layer, k the Boltzmann constant, and T the absolute temperature. The calculated f_c using equation S3 with the parameters in Table S1 fit well the measurements as shown in Fig. S10.

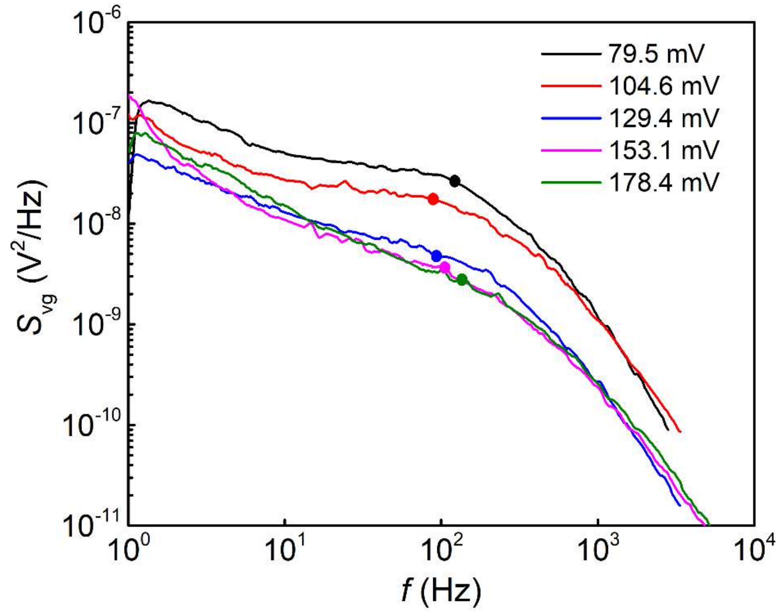

Fig. S10. PSD (solid curves) of Dev. A measured in 10 mM HCl at different gate overdrive $V_G - V_T$. The solid points on the curves are f_c calculated using equation S3.

Supplementary Section 12: Time constants dependence

Interaction between analyte and its DB receptor on a surface can be described by the first-order Langmuir kinetics (*39*, *40*). The fraction of the analyte bound receptors (θ) on the surface is determined by both capture and emission processes through

$$\frac{\mathrm{d}\theta}{\mathrm{d}t} = k_{\mathrm{on}} c_{\mathrm{Hs}} \left(1-\theta\right) - k_{\mathrm{off}} \theta , \tag{S4}$$

where k_{on} and k_{off} are the association and dissociation constants of the analyte-receptor interaction, which is determined by the kinetic energy barriers of the capture (ΔE_{cap}) and emission (ΔE_{emi}) processes, respectively (see the schematic illustration in Fig. 3C (upper)). However, for the H^+-DB interaction in our system, the potential drop across the Stern layer V_{st} will add an additional barrier qV_{st} to the H^+ emission process, as illustrated in Fig. 3C (lower). To include this additional emission barrier into our analysis, equation S4 could be written as

$$\frac{\mathrm{d}\theta}{\mathrm{d}t} = k_{\mathrm{on}} c_{\mathrm{Hs}} \left(1-\theta\right) - k_{\mathrm{off}} e^{-qV_{\mathrm{st}}/kT} \theta . \tag{S5}$$

In the case of a single DB, θ changes from 0 to 1 when an H^+ ion is captured, and from 1 to 0 when the H^+ ion is emitted. Therefore, τ_{c} and τ_{e} of the H^+-DB interaction can therefore be expressed as

$$\frac{1}{\tau_{\mathrm{c}}} = k_{\mathrm{on}} c_{\mathrm{Hs}} , \quad \frac{1}{\tau_{\mathrm{e}}} = k_{\mathrm{off}} e^{-qV_{\mathrm{st}}/kT} . \tag{S6}$$

Supplementary Section 13: Number fluctuation contribution to single charge signal

The contribution of relative change of number fluctuation $\Delta N/N$ is calculated mathematically. Once an H^+ is captured on SiNW surface, the elemental charge will be shared by the capacitances of SiNW and EDL. The induced carrier number in the SiNW is

$$\Delta N = \frac{C_{\mathrm{Si}}}{C_{\mathrm{Si}} + C_{\mathrm{EDL}}} = \frac{C_{\mathrm{Si}}}{C_{\mathrm{Si}} + \dfrac{C_{\mathrm{st}} C_{\mathrm{dif}}}{C_{\mathrm{st}} + C_{\mathrm{dif}}}}, \tag{S7}$$

where C_{Si}, C_{st}, and C_{dif} are the differential capacitances of SiNW, Stern layer, and diffuse layer, respectively. C_{st} is fixed at 4×10^{-5} F cm^{-2} (Table S1). C_{Si} and C_{dif} are calculated as the changes of charge densities divided by the changes of potentials in SiNW and diffuse layer when V_G increases. The total carrier number N in SiNW channel is calculated by integrating the electron density in SiNW channel. The plot of $\Delta N/N$ are presented in Fig. S11. The contribution of number fluctuation $\Delta N/N$ is much lower than the measured single charge signal in Fig. 3E and Fig. 4C.

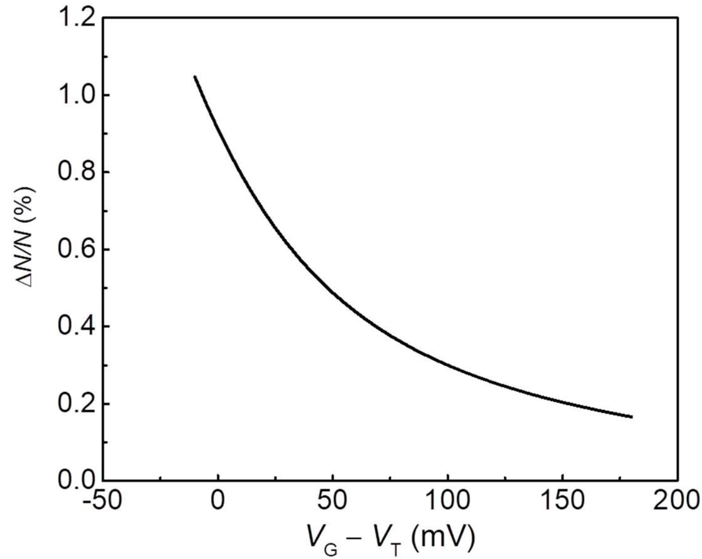

Fig. S11. Calculated results of number fluctuation as a function of $V_G - V_T$.

Supplementary Section 14: Mobility fluctuation contribution to single charge signal

$\Delta I_{DS}/I_{DS}$ is mainly ascribed to $\Delta\mu/\mu$ due to the change of local Coulomb scattering strength induced by a single charge (*37*):

$$\frac{\Delta I_{DS}}{I_{DS}} = \frac{\Delta\mu}{\mu} = \frac{\alpha_{sc}\mu}{A} \quad . \tag{S8}$$

Electron mobility μ is extracted from the transfer curve. Since the SiNWFET works at the linear region (V_{DS} = 10 mV), the on-state current follow

$$I_{DS} = \frac{W\mu C_{EDL}}{L}\left(V_G - V_T - \frac{V_{DS}}{2}\right)V_{DS}, \tag{S9}$$

where C_{EDL} is the capacitance of EDL, which acts as the gate dielectric. C_{EDL} can be obtained from the calculation of the potential and charge distribution in the EDL. The extracted electron mobility using equation S9 is plotted in Fig. S12. At higher V_G, the Coulomb scattering strength will be weakened due to the screen effect (*37*). The scattering coefficient α_{sc} was reported to show the dependence of the carrier density in SiNW (N_{den}) due to the screen effect:

$$\alpha_{sc} = \alpha_1 - \alpha_2 \ln\left(N_{den} / N_{den0}\right). \tag{S10}$$

N_{den} is calculated using the total carrier number in SiNW and surface area of SiNW, *i.e.*, $N_{den} = N/A$. N_{den0} is the reference carrier density for logarithm calculation. Here, N_{den0} is defined as $N_{den0} = 10^{12}$ cm^{-2}. The parameters α_1 and α_2 are extracted by fitting the measured data of $\Delta I_{DS}/I_{DS}$ in Fig. 3E and 4C. α_1 and α_2 and the range of α_{sc} are listed in Table S1.

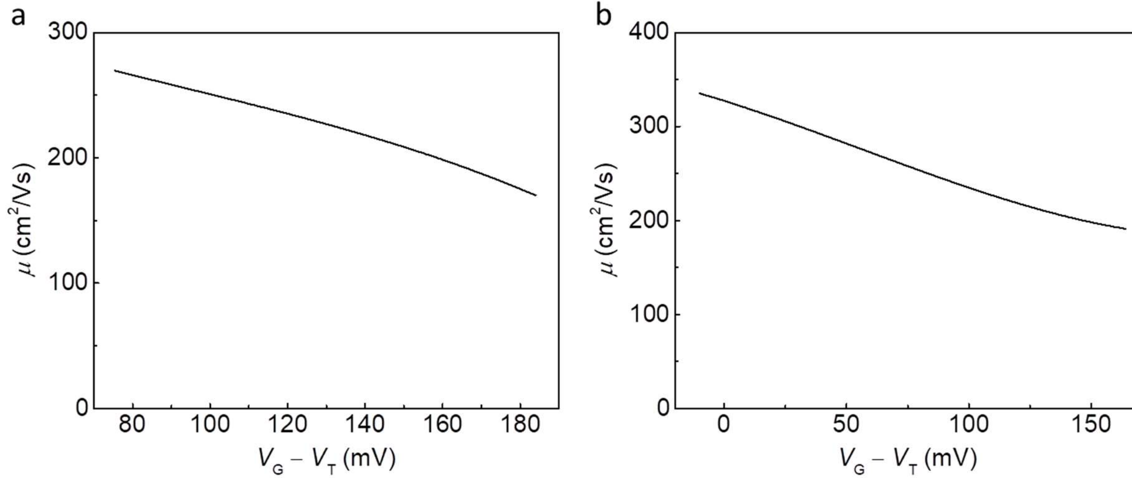

Fig. S12. Extracted electron mobility from transfer curve. Electron mobility of (a) Dev. A and (b) Dev. B as a function of $V_G - V_T$.

Supplementary Section 15: Current histograms of Dev. B at different V_G

The current histograms of DB 1 (left hand side) and DB 2 (right hand side) of Dev. B.

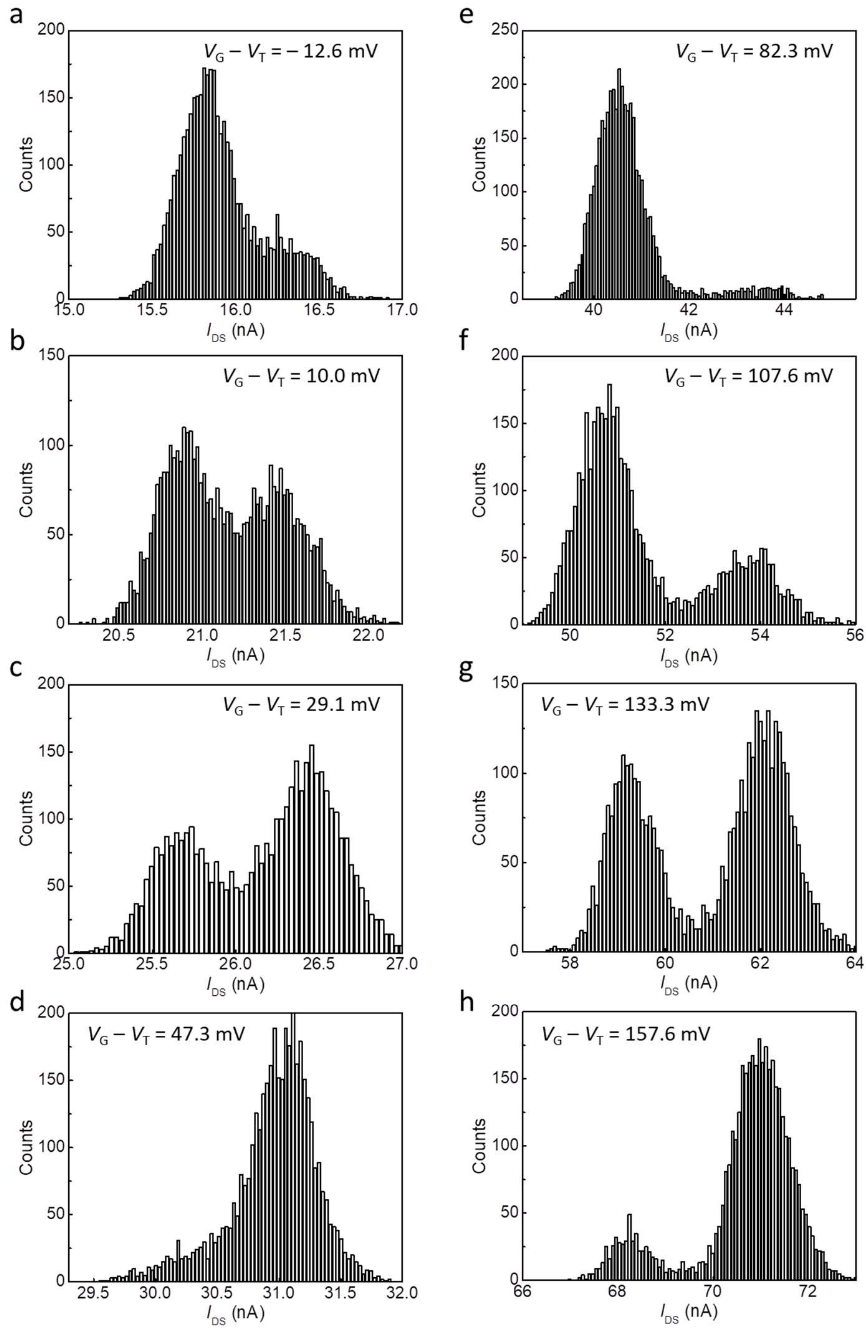

Fig. S13. Histograms of current records listed in Fig. 4A.

Supplementary Section 16: Charge density calculation in the SiNWFETs

In our measurements, V_G is higher or slightly lower than V_T, so the hole density is negligible compared with electron density. The charge density is obtained by solving the Poisson equation in the scaled gate-all-around SiNW (see the schematic of SiNW cross section in Fig. S14a):

$$\frac{d^2\psi}{dx^2} = \frac{q}{\varepsilon}\left(n + N_A\right), n = n_0 e^{\frac{\psi}{kT}}, \tag{S11}$$

where ψ is the potential in SiNW, q the elemental charge, ε the dielectric constant of Si, n the electron density, N_A the acceptor density ($N_A = 10^{15}$ cm^{-3}), n_0 the equilibrium density of electron ($n_0 = 10^5$ cm^{-3}), k the Boltzmann constant, T the temperature. Since the SiNW is central-symmetric, the Poisson equation is solved in one side ($0 < x < r$). At SiNW surface ($x = r$), the boundary condition is $\psi = \psi_{Si}$, and at SiNW central ($x = 0$), the boundary condition is $d\psi/dx = 0$. Once the potential distribution is solved, the net charge density in SiNW σ_{Si} is obtained by Gaussian law:

$$\sigma_{Si} = -\varepsilon \frac{d\psi}{dx}|_{x=r}. \tag{S12}$$

The Poisson equation and net charge density is solved numerically by Matlab. For a direct comparison with the surface charge density, the net charge density in SiNW averaged by $r(|\sigma_{Si}/r|)$ is plotted as a function of ψ_{Si}, in Fig. S14b. The correction factor γ is defined as the ratio of the surface charge density and the average charge density, and the calculated results of γ (black dots) is fitted well with $\gamma = 0.978 + 1.72\times\exp(0.0256\times\psi_{Si})$ (black curve).

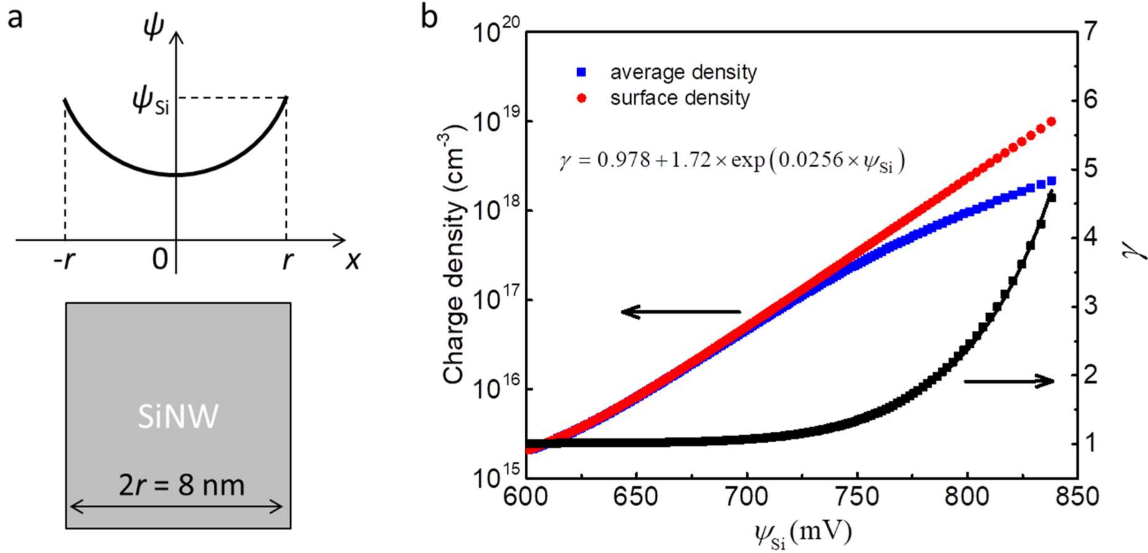

Fig. S14. Charge density calculation and correction in a SiNWFET. (a) Schematic potential distribution in the SiNW cross section. (b) Calculated charge density as a function of surface potential. The average charge density can be expressed as the surface charge density divided by the correction factor.

Table S1.

Parameters extracted from the fitting of single H^+-DB interaction kinetics and signal amplitudes of Dev. A and B.

Parameters	Dev. A	Dev. B (DB1)	Dev. B (DB2)
C_{st} (F cm^{-2})	4.0×10^{-5}	4.0×10^{-5}	4.0×10^{-5}
k_{on} (M^{-1} ms^{-1})	0.10	0.05	0.10
k_{off} (ms^{-1})	0.20	1.4	0.15
α_{sc} (V s)	$5.4–8.4\times10^{-15}$	$2.7–2.8\times10^{-15}$	$5.8–8.5\times10^{-15}$
α_1 (V s)	1.3×10^{-14}	2.8×10^{-15}	1.2×10^{-14}
α_2 (V s)	3.1×10^{-15}	1.0×10^{-16}	3.0×10^{-15}

REFERENCES AND NOTES

1. W. Gao, S. Emaminejad, H. Y. Y. Nyein, S. Challa, K. Chen, A. Peck, H. M. Fahad, H. Ota, H. Shiraki, D. Kiriya, D.-H. Lien, G. A. Brooks, R. W. Davis, A. Javey, Fully integrated wearable sensor arrays for multiplexed in situ perspiration analysis. *Nature* **529**, 509–514 (2016).

2. Y. Cui, Q. Wei, H. Park, C. M. Lieber, Nanowire nanosensors for highly sensitive and selective detection of biological and chemical species. *Science* **293**, 1289–1292 (2001).

3. H.-M. So, K. Won, Y. H. Kim, B.-K. Kim, B. H. Ryu, P. S. Na, H. Kim, J.-O Lee, Single-walled carbon nanotube biosensors using aptamers as molecular recognition elements. *J. Am. Chem. Soc.* **127**, 11906–11907 (2005).

4. A. Star, E. Tu, J. Niemann, J.-C. P. Gabriel, C. S. Joiner, C. Valcke, Label-free detection of DNA hybridization using carbon nanotube network field-effect transistors. *Proc. Natl. Acad. Sci. U.S.A.* **103**, 921–926 (2006).

5. J. Salfi, I. G. Savelyev, M. Blumin, S. V. Nair, H. E. Ruda, Direct observation of single-charge-detection capability of nanowire field-effect transistors. *Nat. Nanotechnol.* **5**, 737–741 (2010).

6. N. K. Rajan, D. A. Routenberg, M. A. Reed, Optimal signal-to-noise ratio for silicon nanowire biochemical sensors. *Appl. Phys. Lett.* **98**, 264107–2641073 (2011).

7. S. Sorgenfrei, C.-Y. Chiu, R. L. Gonzalez, Jr, Y.-J. Yu, P. Kim, C. Nuckolls, K. L. Shepard, Label-free single-molecule detection of DNA-hybridization kinetics with a carbon nanotube field-effect transistor. *Nat. Nanotechnol.* **6**, 126–132 (2011).

8. S. Sorgenfrei, C.-Y. Chiu, M. Johnston, C. Nuckolls, K. L. Shepard, Debye screening in single-molecule carbon nanotube field-effect sensors. *Nano Lett.* **11**, 3739–3743 (2011).

9. J. Li, G. He, H. Ueno, C. Jia, H. Noji, C. Qi, X. Guo, Direct real-time detection of single proteins using silicon nanowire-based electrical circuits. *Nanoscale* **8,** 16172–16176 (2016).

10. N. Singh, K. D. Buddharaju, S. K. Manhas, A. Agarwal, S. C. Rustagi, G. Q. Lo, N. Balasubramanian, D.-L. Kwong, Si, SiGe nanowire devices by top–down technology and their applications. *IEEE Trans. Electron. Devices* **55,** 3107–3118 (2008).

11. I. Park, Z. Li, A. P. Pisano, R. S. Williams, Top-down fabricated silicon nanowire sensors for real-time chemical detection. *Nanotechnology* **21**, 015501 (2010).

12. S. Chen, J. G. Bomer, E. T. Carlen, A. van den Berg, Al_2O_3/silicon nanoISFET with near ideal Nernstian response. *Nano Lett.* **11**, 2334–2341 (2011).

13. M. Wipf, R. L. Stoop, A. Tarasov, K. Bedner, W. Fu, I. A. Wright, C. J. Martin, E. C. Constable, M. Calame, C. Schönenberger, Selective sodium sensing with gold-coated silicon nanowire field-effect transistors in a differential setup. *ACS Nano* **7**, 5978–5983 (2013).

14. O. Knopfmacher, A. Tarasov, W. Fu, M. Wipf, B. Niesen, M. Calame, C. Schönenberger, Nernst limit in dual-gated Si-nanowire FET sensors. *Nano Lett.* **10**, 2268–2274 (2010).

15. K. Martens, S. Santermans, M. Gupta, G. Hellings, R. Wuytens, B. D. Bois, E. Dupuy, E. Altamirano-Sanchez, K. Jans, R. Vos, T. Stakenborg, L. Lagae, M. Heyns, S. Severi, W. V. Roy, BioFET technology: Aggressively scaled pMOS FinFET as biosensor, in *Proceedings of the 2019 IEEE International Electron Devices Meeting (IEDM)*, San Francisco, CA, USA, 7 to 11 December 2019.

16. E. Stern, J. F. Klemic, D. A. Routenberg, P. N. Wyrembak, D. B. Turner-Evans, A. D. Hamilton, D. A. LaVan, T. M. Fahmy, M. A. Reed, Label-free immunodetection with CMOS-compatible semiconducting nanowires. *Nature*, **445**, 519–522 (2007).

17. N. Clément, K. Nishiguchi, J. F. Dufreche, D. Guerin, A. Fujiwara, D. Vuillaume, A silicon nanowire ion-sensitive field-effect transistor with elementary charge sensitivity. *Appl. Phys. Lett.* **98**, 014104 (2011).

18. E. Simoen, C. Claeys, On the flicker noise in submicron silicon MOSFETs. *Solid State Electron.* **43**, 865–882 (1999).

19. C. G. Theodorou, E. G. Ioannidis, F. Andrieu, T. Poiroux, O. Faynot, C. A. Dimitriadis, G. Ghibaudo, Low-frequency noise sources in advanced UTBB FD-SOI MOSFETs. *IEEE Trans. Electron. Devices* **61**, 1161–1167 (2014).

20. M. J. Deen, M. W. Shinwari, J. C. Ranuárez. Noise considerations in field-effect biosensors. *J. Appl. Phys.* **100**, 074703 (2006).

21. S. Bangsaruntip, G. M. Cohen, A. Majumdar, Y. Zhang, S. U. Engelmann, N. C. M. Fuller, L. M. Gignac, S. Mittal, J. S. Newbury, M. Guillorn, T. Barwicz, L. Sekaric, M. M. Frank, J. W. Sleight, High performance and highly uniform gate-all-around silicon nanowire MOSFETs with wire size dependent scaling, in *Proceedings of the 2019 IEEE International Electron Devices Meeting (IEDM)*, Baltimore, MD, USA, 7 to 9 December 2009.

22. S.-W. Ryu, K. Min, J. Shin, H. Kwon, D. Nam, T. Oh, T.-S. Jang, M. Yoo, Y. Kim, S. Hong, Overcoming the reliability limitation in the ultimately scaled DRAM using silicon migration technique by hydrogen annealing, in *Proceedings of the 2017 IEEE International Electron Devices Meeting (IEDM)*, San Francisco, CA, USA, 2 to 6 December 2017.

23. S. Zafar, C. D'Emic, A. Jagtiani, E. Kratschmer, X. Miao, Y. Zhu, R. Mo, N. Sosa, H. Hamann, G. Shahidi, H. Riel, Silicon nanowire field effect transistor sensors with minimal sensor-to-sensor variations and enhanced sensing characteristics. *ACS Nano* **12**, 6577–6587 (2018).

24. A. H. Edwards, Interaction of H and H_2 with the silicon dangling orbital at the 〈111〉 Si/SiO_2 interface. *Phys. Rev. B Condens. Matter* **44**, 1832–1838 (1991).

25. G. W. Trucks, K. Raghavachari, G. S. Higashi, Y. J. Chabal, Mechanism of HF etching of silicon surfaces: A theoretical understanding of hydrogen passivation. *Phys. Rev. Lett.* **65**, 504–507 (1990).

26. E. Yablonovitch, D. L. Allara, C. C. Chang, T. Gmitter, T. B. Bright, Unusually low surface-recombination velocity on silicon and germanium surfaces. *Phys. Rev. Lett.* **57**, 249–252 (1986).

27. Z. Shi, J.-P. Mieville, M. Dutoit, Random telegraph signals in deep submicron n-MOSFET's. *IEEE Trans. Electron. Devices* **41**, 1161–1168 (1994).

28. J. Li, S. Pud, M. Petrychuk, A. Offenhäusser, S. Vitusevich, Sensitivity enhancement of Si nanowire field effect transistor biosensors using single trap phenomena. *Nano Lett.* **14**, 3504–3509 (2014).

29. P. M. Lenahan, T. D. Mishima, J. Jumper, T. N. Fogarty, R. T. Wilkins, Direct experimental evidence for atomic scale structural changes involved in the interface-trap transformation process. *IEEE Trans. Nucl. Sci.* **48**, 2131–2135 (2001).

30. O. Stern, Zur theorie der elektrolytischen doppelschicht. *Z. Elektrochem. Angew. Phys. Chem.* **30**, 508–516 (1924).

31. R. E. G. van Hal, J. C. T. Eijkel, P. Bergveld, A novel description of ISFET sensitivity with the buffer capacity and double-layer capacitance as key parameters. *Sens. Actuators B* **24**, 201–205 (1995).

32. D. Landheer, G. Aers, W. R. McKinnon, M. J. Deen, J. C. Ranuarez, Model for the field effect from layers of biological macromolecules on the gates of metal-oxide-semiconductor transistors. *J. Appl. Phys.* **98**, 044701 (2005).

33. M. J. Kirton, M. J. Uren, Noise in solid-state microstructures: A new perspective on individual defects, interface states and low-frequency ($1/f$) noise. *Adv. Phys.* **38**, 367–468 (1989).

34. R. E. G. van Hal, J. C. T. Eijkel, P. Bergveld, A general model to describe the electrostatic potential at electrolyte oxide interfaces. *Adv. Colloid Interface Sci.* **69**, 31–62 (1996).

35. D. Landheer, W. R. McKinnon, G. Aers, W. Jiang, M. J. Deen, M. W. Shinwari, Calculation of the response of field-effect transistors to charged biological molecules. *IEEE Sens. J.* **7**, 1233–1242 (2007).

36. S. T. Martin, G. P. Li, E. Worley, J. White, The gate bias and geometry dependence of random telegraph signal amplitudes [MOSFET]. *IEEE Electron. Device Lett.* **18**, 444–446 (1997).

37. K. K. Hung, P. K. Ko, C. Hu, Y. C. Cheng, A unified model for the flicker noise in metal-oxide-semiconductor field-effect transistors. *IEEE Trans. Electron. Devices* **37,** 654–665 (1990).

38. R. Jayaraman, C. G. Sodini, A 1/*f* noise technique to extract the oxide trap density near the conduction band edge of silicon. *IEEE Trans. Electron. Devices* **36**, 1773–1782 (1989).

39. Y. Liu, L. Shen, From Langmuir kinetics to first- and second-order rate equations for adsorption. *Langmuir* **24**, 11625–11630 (2008).

40. T. M. Squires, R. J. Messinger, S. R. Manalis, Making it stick: Convection reaction and diffusion in surface-based biosensors. *Nat. Biotechnol.* **26**, 417–426 (2008).